Heat transfer and material flow during laser assisted multi-layer additive manufacturing

V. Manvatkar, A. De, and T. DebRoy
Department of Materials Science and Engineering, The Pennsylvania State University, University Park, Pennsylvania 16802, USA

(Received 15 August 2014; accepted 18 September 2014; published online 29 September 2014)

A three-dimensional, transient, heat transfer, and fluid flow model is developed for the laser assisted multilayer additive manufacturing process with coaxially fed austenitic stainless steel powder. Heat transfer between the laser beam and the powder particles is considered both during their flight between the nozzle and the growth surface and after they deposit on the surface. The geometry of the build layer obtained from independent experiments is compared with that obtained from the model. The spatial variation of melt geometry, cooling rate, and peak temperatures is examined in various layers. The computed cooling rates and solidification parameters are used to estimate the cell spacings and hardness in various layers of the structure. Good agreement is achieved between the computed geometry, cell spacings, and hardness with the corresponding independent experimental results. © *2014 AIP Publishing LLC*. [http://dx.doi.org/10.1063/1.4896751]

I. INTRODUCTION

Laser assisted additive manufacturing is a potentially attractive process for the manufacture of near net shape parts from a stream of alloy powder in aerospace, automotive, medical, and other industries.[1] However, the process requires careful control of laser power, power density, scanning speed, powder feed rate, size distribution, and other variables in order to achieve an acceptable quality of the parts.[2–4] Furthermore, the scale and morphology of the solidification structure, microstructure, mechanical properties, and defects also are affected by the process variables.[5] Selection of variables by trial and error is time consuming and expensive and limits wider industrial usage of the additive manufacturing process. What is necessary and not currently available is a reliable, well-tested, phenomenological process model that can serve as a basis for the selection of important process variables to produce defect free, structurally sound, and reliable parts made by the additive manufacturing process based on scientific principles.

Many simultaneously occurring physical processes[6–8] affect the structure and properties of the parts in the laser assisted additive manufacturing process. A stream of powder interacts with the laser beam prior to their deposition on the substrate. The deposited particles rapidly form a molten pool on the surface of the growing layer and the solidification of the molten region forms the structure when the laser beam moves forward.[9] A significant spatial gradient of temperature drives a strong convective flow of liquid metal due to Marangoni effect and facilitates convective heat transfer within the molten pool.[6–8,10] The solidified material undergoes multiple heating and cooling cycles as layers of new alloys are deposited on the previously deposited layers.[11–14] These thermal cycles affect the evolution of microstructure and mechanical properties of the deposited layers.[15–17] An understanding of the details of heat transfer, liquid metal flow, cooling rates, and other solidification parameters is essential for the control of microstructure and properties of the deposited layer based on scientific principles.

Numerical models of heat and mass transfer and fluid flow have provided unique insight into the complex laser welding processes. However, these models cannot be used for understanding the additive manufacturing process because there are several important differences between the two processes. Interaction of the powder with the laser beam, progressive build-up of the layers, multiple thermal cycles at any specific location as new layers are added on the previously deposited layers, transient changes in the geometry of the part are some of the differences that preclude the use of existing models of welding to understand the additive manufacturing process.

Here, we report the development of a comprehensive, three-dimensional, transient, heat transfer, and fluid flow model for the laser assisted additive manufacturing of parts from a stream of alloy powders. The model solves the equations of conservation of mass, momentum, and energy with appropriate boundary conditions and temperature dependent properties of materials in different regions of the system. The interaction between the laser beam and the powder particles during their flight and subsequently when they are added to the build surface is considered in the calculations. The outputs from the model are the temperature and velocity fields, cooling rates, and solidification parameters. The model is validated by comparing several experimentally determined parameters with the corresponding theoretically calculated results. For example, the geometry of the deposited structure is compared with that computed from the model for the deposition of a multi-layered structure of an austenitic stainless steel. Furthermore, the experimentally determined scale of the solidification structure and hardness data are compared with the corresponding theoretically determined values from the modeling results. After validation, the model is used to investigate the spatial variations of peak temperatures, cooling rates, and solidification parameters during build-up of a multilayer austenitic stainless steel structure.

II. PROGRESS MADE IN PREVIOUS RESEARCH

Several useful previous works serve as a foundation for the work reported in this paper. For example, the work by Grujicic *et al.*[18] shows the importance of laser-material interaction during flight of the particles between the nozzle and the growth surface. He and Mazumder[6] estimated temperature rise of the powders during laser-powder interaction using heat balance. After the particles impinge on the depositing layer, their absorption of the laser beam is affected by the particle size, the depth of the particle layer, and their chemical composition.[9] The addition of powder particles during deposition results in the transient growth of the depositing layer along both the scanning and vertical directions. Previous research has shown that the addition of mass could be simulated by progressive activation of elements in the computational domain. Similarly, the addition of heat both due to the impinging preheated powder particles and the direct absorption of the laser beam by the growing layer could be represented by an appropriate Gaussian energy density distribution over a surface or volume or both.[6,7,12–14,17,19,20]

Transient temperature fields, residual stresses, and distortions have been the focus of most of the previous modeling works, including those by Neela and De,[12] Manvatkar *et al.*[13] and Wang and Felicelli.[14] They used commercial finite element software for the analysis of heat conduction and stresses to examine the role of various variables. These calculations do not consider convective heat transfer in the liquid region which is often the main mechanism of heat transfer. Consequently, the computed peak temperatures and temperature gradients are significantly overestimated, since the mixing of the hot and cold fluids is not considered. Cooling rate which is the product of temperature gradient and the scanning velocity is also significantly overestimated.

Comprehensive calculations of transient heat transfer and fluid flow during additive manufacturing are just beginning. The initial two-dimensional calculations[21,22] of heat transfer and fluid flow were followed by adaptation of transient, three-dimensional models of laser cladding,[6,7,19,20] and welding[23] to additive manufacturing. Tracking of the free surface was also simulated by the level set method[6,7,19,20,22] which is computationally highly intensive. Furthermore, the quality of the calculations remains to be tested by comparison with any transient experimental tracking of the topology of the free surface.

In summary, the previous studies have established the benefits of numerical simulation of heat transfer and fluid flow during additive manufacturing and demonstrated the need to develop transient three dimensional models incorporating additions of heat and mass in a manner that is computationally tractable. At the same time, the calculations have to be verified by comparison with measurements of build geometry and metallurgical parameters.

III. HEAT TRANSFER AND FLUID FLOW MODEL

The model calculates transient, three-dimensional, temperature, and velocity fields from process variables, such as the laser power, power density distribution, scanning speed, and powder feeding variables, such as the chemical composition, particle size, feed rate, and velocity of the powder particles. The physical processes considered in the calculations are described below.

A. Assumptions

Several simplifying assumptions are made to make the complex, three-dimensional, transient calculations tractable. The densities of the solid and liquid metals are assumed to be constant. The surface of the growing layer is assumed to be flat. The loss of alloying elements due to vaporization and its effects on both the heat loss and composition change are not considered in the calculations.

B. Particle/laser beam interaction

After emerging from the powder feeding nozzle, the particles are heated during flight prior to their transfer to the depositing surface. The heat absorbed by the particles during flight depends on the residence time of the particles, particle size, gas velocity, material properties, and laser power density. The following approximate heat balance is conducted to estimate the temperature rise of the particles during their flight assuming that the particles are spherical in shape

$$\Delta T = \frac{\eta_m \times \eta_s \times \frac{P}{\pi r_b^2} \times \left(2\pi r_p^2\right)\tau}{\left(4/3 \times \pi \times r_p^3\right) \times C_p \times \rho_p}, \tag{1}$$

where ΔT is the average in-flight temperature rise of the powder particles, P is the laser power, r_b and r_p are the laser beam radius and the average radius of the particles, respectively, C_P is the specific heat, η_m is an interference factor to account for shielding of some particles from the laser beam by other particles, η_s is the fraction of available laser power absorbed by the solid particles, τ is the time of flight which depends on the velocity of particles and the distance between the nozzle and the depositing surface, i.e., the length of flight, and ρ_P is the density of the particles. The upper hemisphere of the spherical particle surface is directly exposed to the laser beam. As a result, the absorption of the laser beam occurs on half of the total surface area ($2\pi r_P^2$) which appears in the numerator of Eq. (1). After the particles are deposited on the depositing surface they continue to absorb laser beam energy efficiently. The rate of absorption of laser beam energy by the powder bed is calculated based on previous work on the absorption of laser beam energy by the powder bed.[9] The amount of laser power absorbed by the depositing surface, P_s, is given by

$$P_s = \eta_l \times (1 - \eta_p) \times P, \tag{2}$$

where η_p is the fraction of the laser power absorbed by the powder in-flight and η_l is the fraction of available laser power absorbed by the growing layer. Its value is high when the powder is still solid, but a short time (a few milliseconds) after the heated particles arrive on the growing layer, they melt and then the liquid surface absorbs energy by Fresnel absorption.[13] So, the value of η_l is high initially when the liquid layer is forming but reduces once the surface melts. When the material is in powder form, the laser beam

TABLE I. Data used for numerical simulations. The laser material interaction length is the distance between the point, where material powders are introduced into the laser beam and the top surface of the layer being deposited.

Process parameter	Value
Substrate size (mm × mm × mm)	10 × 3.1 × 4
Deposited layer size	4 × 0.72 × 0.38
Laser power (W)	210
Laser scanning speed (mm s^{-1})	12.7
Laser beam diameter (mm)	0.9
Idle time (s)	0.03
Laser distribution factor	3
Material flow rate (g min^{-1})	25
Material powder size (μm)	175
Laser material interaction length (mm)	2
Particle velocity (mm s^{-1})	2.4
Carrier gas flow rate (l min^{-1})	4

undergoes multiple reflections within the powder layers. As a result, the coefficient of laser beam absorption by the powder bed is higher than the absorption coefficient of the liquid.

The energy absorbed by the powder and the growing layer is used as a source term in the energy conservation equation as follows:

$$S_i = \frac{Pd}{\pi r_b^2 t}\left[\eta_p + \eta_l\left(1-\eta_p\right)\right]\exp\left(-d\frac{r^2}{r_b^2}\right), \tag{3}$$

η_p is fraction of laser energy absorbed by the powder during flight, P is laser power, d is laser energy distribution factor, t is layer thickness, and r is radial distance from laser beam axis. The layer thickness, t, is determined experimentally. The two terms within the square bracket represent the fraction of laser energy transferred to the particles during their flight through the beam and the irradiation of beam on the depositing surface, respectively. The exponential term accounts for the Gaussian distribution of laser energy as a function of distance from the axis of the beam.

C. Governing equations

The model solves the conservation equations for mass, momentum, and energy in transient three-dimensional form. These equations are available in standard text books[24] and in many of our previous publications[25,26] and are not repeated here. The specific discretization scheme and the solution methodology for transient three dimensional form are also discussed in details in the literature.[24,26] Only the special features of the calculations are discussed here. The process parameters and material properties used for numerical calculations are presented in Tables I and II, respectively.

D. Computational domain and the boundary conditions

The transient heat transfer and fluid flow calculations are performed for a rectangular solution domain representing the substrate, deposited layers, and the surrounding gas shown in Fig. 1. In order to expedite calculations, advantage is taken of the geometrical symmetry of the deposited layers along the mid-width longitudinal plane and calculations are done only in one half of each layer. The deposition is simulated through discrete time steps. At the beginning of the simulation, all the cells above the substrate are assigned properties of an inert gas and the initial temperature of the domain is taken as the room temperature (298 K). The moving heat source is simulated by progressively shifting of the laser beam axis by a very short predetermined distance, X_s, in the direction of deposition equal to a small fraction of the laser beam diameter. The corresponding time step, Δt, is calculated from the scanning velocity, v

$$\Delta t = X_s/v. \tag{4}$$

During each shift, the properties of the computational cells representing the volume of the deposited material are changed from the properties of the gas to that of the deposit material. At the end of each layer, an idle time is provided to allow the laser beam to move to the initial location prior to

TABLE II. Material properties used for numerical simulations. The absorption coefficient values in the table are for 1.06 μm wavelength laser beam.

Material properties	Values	References
Properties of SS316		
Density (kg mm^{-3})	7800	27
Solidus temperature (K)	1693	27
Liquidus temperature (K)	1733	27
Thermal conductivity (W m^{-1} K^{-1})	$11.82 + 0.0106\,T$	27
Specific heat (J kg^{-1} K^{-1})	$330.9 + 0.563\,T - 4.015 \times 10^{-4}\,T^2 + 9.465 \times 10^{-8}T^3$	27
Latent heat of fusion (J kg^{-1})	2.67×10^5	27
Coefficient of thermal expansion (K^{-1})	1.9×10^{-5}	27
Viscosity of liquid alloy (kg m^{-1} s^{-1})	6.7×10^{-3}	27
Temperature coefficient of surface tension (N m^{-1} K^{-1})	-0.4×10^{-3}	29
Absorption coefficient in solid/liquid (η_s,η_l)	0.3	9
Absorption coefficient in powder bed (η_P)	0.7	9
Interference factor (η_m)	1.0	…
Properties of argon		
Density (kg mm^{-3})	0.974	28
Specific heat (J kg^{-1} K^{-1})	520	28
Thermal conductivity (W m^{-1} K^{-1})	26.41×10^{-3}	28

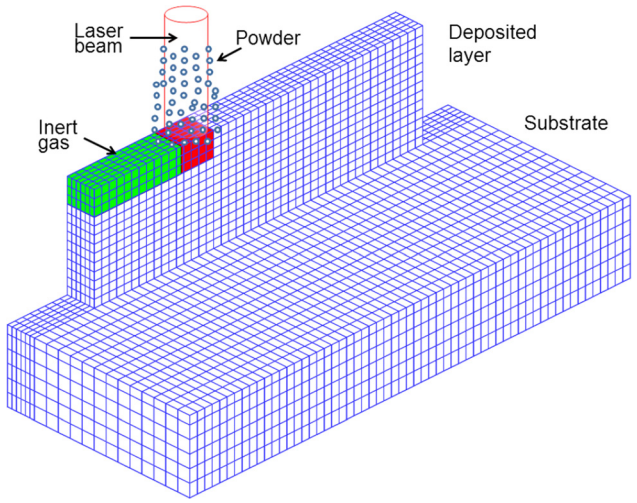

FIG. 1. A schematic representation of the solution domain.

the deposition of the next layer. The idle time is the time gap necessary for the laser beam to travel between the end of one layer and the beginning of the next upper layer. The laser beam is switched off and no material is deposited during this time. The aforementioned procedure is repeated till the deposition of all the layers.

The variation of all variables across the mid-section longitudinal symmetry plane is set to zero. In the remaining surfaces, heat loss by radiation and convection is applied as boundary conditions for the solution of the enthalpy equation. For the solution of the momentum equations, the longitudinal and transverse velocities at the melt pool surface boundary were related to the corresponding velocities in locations just below the surface through Marangoni boundary conditions.[25]

E. Grid spacing, time steps and convergence of the solution

Spatially non-uniform grids, with finer grid spacing near the axis of the laser beam were used for efficient calculation of variables. A computational domain, 10 mm in length, 3.1 mm wide, and 5.5 mm in height, was considered and divided into $160 \times 29 \times 37$ or 171 680 grid points. The duration of the time step is decided using Eq. (4).

The governing equations were discretized by following a control volume method.[24] The velocity components and the scalar variables were stored at different locations to enhance the convergence and stability of the computational scheme. At each time step, the three components of velocities and the enthalpy were iterated following a sequence known as the SIMPLE algorithm.[24] The implicit computational scheme adapted is unconditionally stable. The discretized linear equations were solved using a Gaussian elimination technique known as the tri-diagonal matrix algorithm.[24] At any given time step, the iterations were terminated when two convergence criteria were satisfied. The magnitudes of the residuals of enthalpy and the three components of velocities, and the overall heat balance were checked after every iteration. The largest imbalance of any variable on the two sides of a discretization equation for all interior grid points had to be less than 0.1%. In addition, the overall heat balance criterion required that the sum of the total heat loss from the domain and the heat accumulation had to be almost equal to the heat input into the calculation domain. Their difference had to be less than 0.5% of the heat input for this convergence criterion to be satisfied. The criteria were selected so that the final results were not adversely affected while maintaining computational speed. Typically a total of 26 000 iterations were necessary per layer and a total of 13.5 billion linear equations were solved cumulatively for all time steps for a three layer structure.

F. Cell spacing and hardness calculations

Cooling rate in the solidification temperature range (1733 K–1693 K) is calculated from the computed temperature at several locations for every layer. The layer wise variation of the secondary dendrite arm spacing is calculated considering the average cooling rate in every layer using the following expression:[13,30]

$$\lambda_2 = A(CR)^{-n}, \tag{5}$$

where λ_2 is secondary dendritic arm spacing (SDAS) in μm, CR is cooling rate in K/s, and A and n are material specific constants having values of 80 and 0.33, respectively. SDAS is the smallest dimension in a typical columnar dendritic microstructure. Experimental observations revealed very fine cellular microstructure in the range of 3–10 μm, in such layer wise deposited structure.[13,30] Manvatkar *et al.*[13] showed that Eq. (5) fits well for predicting cell spacing in very fine cellular structure. Further layer wise yield strength is estimated using a Hall-Petch like relationship presented in Eq. (6) and replacing the grain size by cell spacings as suggested by Manvatkar *et al.*[13]

$$\sigma_y = \sigma_0 + k_y(d_g)^{-0.5}, \tag{6}$$

where σ_y is yield strength, σ_0 is lattice resistance, k_y is grain boundary resistance, and d_g is grain size replaced by cell spacing. The values of σ_0 and k_y used for calculations are 150 MPa and 575 MPa $(\mu m)^{0.5}$. The layer wise hardness (H_V) from yield strength (σ_y) is estimated as

$$H_v = 3\sigma_y(0.1)^{2-m}, \tag{7}$$

where H_V is in kg mm^{-2} and m is Mayer exponent with value 2.25 for steels.[13,31–34]

IV. RESULTS AND DISCUSSION

Figure 2 shows the computed melt pool geometry in the first, second, and third layers deposited for the experimental conditions presented in Table I. Each color band in the profile represents a temperature range shown in the legend. The green colored regions in all the figures indicate that the deposited material reached solidus temperature of the SS316 alloy (1693 K). The vectors show the computed velocity fields in the molten region. A reference vector is shown by an arrow and a comparison of the length of this arrow with

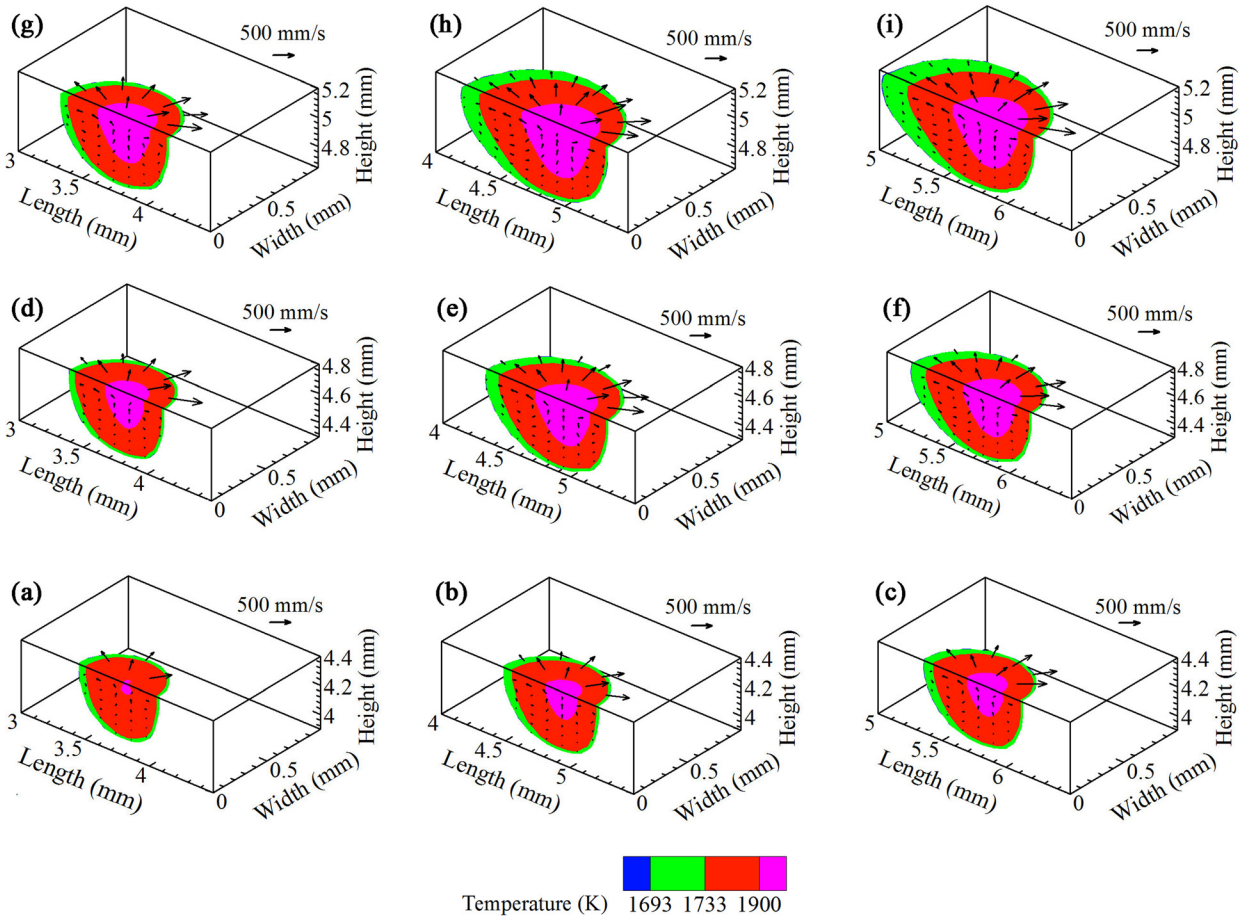

FIG. 2. Evolution of the melt pool geometry in the first three layers. (a)–(c) show the progression of deposition in the first layer, (d)–(f) show changes in the melt pool geometry in the second layer, and (g)–(i) show the same in the third layer.

the vectors shown in the plots reveals the magnitudes of the computed velocities. The velocities are larger at the surface than in the interior because the motion of the liquid metal in the molten region originates at the surface owing to the Marangoni convection. The Marangoni stress results from the spatial gradient of surface tension because of the temperature variation. The computed surface velocities are somewhat higher than 500 mm/s which is comparable with what is reported for laser welding. At these velocities, the computed Pe for heat transfer which represents the ratio of heat transported by convection to that by conduction is much higher than 1 indicating convective heat transfer to be the main mechanism of heat transfer. Consequently, many of the conclusions made by heat conduction calculations need to be revised.

The transverse sections of the computed melt pool profiles in the first three layers are shown in Fig. 3 to examine the geometry of the build. This figure also shows a comparison between the numerically simulated and the corresponding experimentally observed transverse sections for the three layer structure. The good agreement between the two geometries indicates that the model is capable of predicting the correct geometry of the build layers.

Figure 4 shows the computed thermal cycles at three monitoring locations, each at mid-length and mid-height within the first, second, and third layers. Each thermal cycle shows the expected recurrent spikes. The first spike in the thermal cycle for a particular layer shows the peak temperature corresponding to the laser beam positioned above the monitoring location. The subsequent peaks correspond to the positioning of laser above the monitoring location in subsequent passes of the laser as the upper layers are deposited. Thus, the thermal cycles are indicative of the progress of

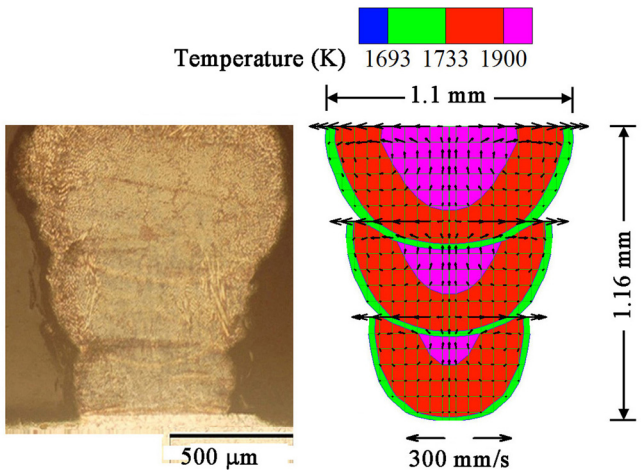

FIG. 3. Comparison of the experimental[13] and theoretical transverse section of the three layer structure.

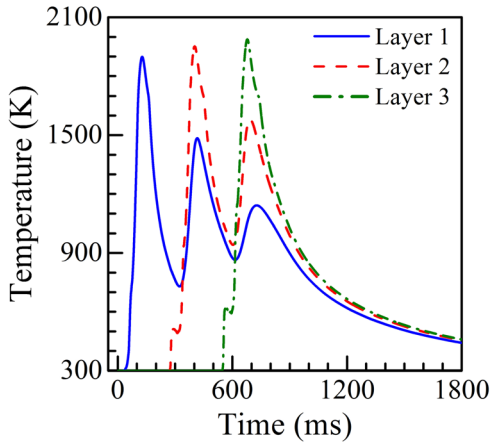

FIG. 4. Thermal cycles at three monitoring locations in the first three layers.

deposition during the process. The peak temperatures experienced by the first, second, and the third layers are 1946 K, 1998 K and 2035 K, respectively. The rise in the peak temperature from the first layer to the second layer is 52 K. However, this rise is reduced to 37 K from the second to the third layer. The first layer can efficiently transfer heat into the substrate because the substrate is cold initially and close to the deposited layer. Thus, the substrate can effectively act as an efficient heat sink. During the deposition of the subsequent top layers, the peak temperature rises as the distance between the substrate and the build layer increases and the new layers are deposited on the previously deposited hot layers. However, the increase slows down with the progressive deposition of subsequent layers, since the heat loss also increases with higher temperatures in the deposited layers.

The computed peak temperatures in various layers are plotted in Fig. 5. The increase in peak temperate in the upper layers owing to the progressively diminished heat extraction by the substrate is clearly observed in the figure. The computed peak temperatures are also compared with those obtained from an independent heat conduction calculations[13] in the figure. As expected, the rise in the peak temperature is more pronounced in the conduction model because the heat

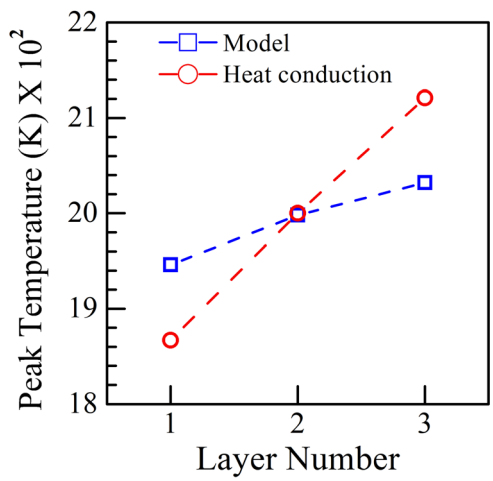

FIG. 5. Comparison of the computed peak temperatures at three monitoring locations within the three layers with those independently reported using a heat conduction model.[13]

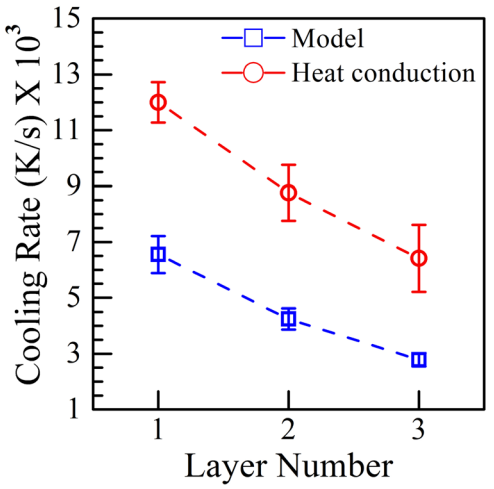

FIG. 6. Variation of cooling rate at three monitoring locations in the three layers. The results of the heat conduction calculations are from the literature.[13]

transfer by convection is ignored and the diminished heat transfer rate leads to rapid increase in temperature.

Fig. 6 shows that the computed cooling rates diminish from 6548 K/s in the first layer to 4245 K/s in the second layer and further to 2779 K/s in the third layer. The average cooling rates independently estimated using a heat conduction model were approximately 12 000 K/s and 6000 K/s in the first and third layers, respectively. These values are unrealistically high because mixing of the hot and the cold liquids that reduce the temperature gradients in the melt pool is ignored in the heat conduction calculations. Since the cooling rate is the product of temperature gradient and the scanning velocity, the cooling rate decreases when the temperature gradient is reduced owing to mixing.

The ratio of the temperature gradient G and the solidification growth rate R affects the solidification morphology. The constitutional supercooling criterion for plane front solidification is given by the following:

$$G/R \geq \Delta T_E/D_L, \tag{8}$$

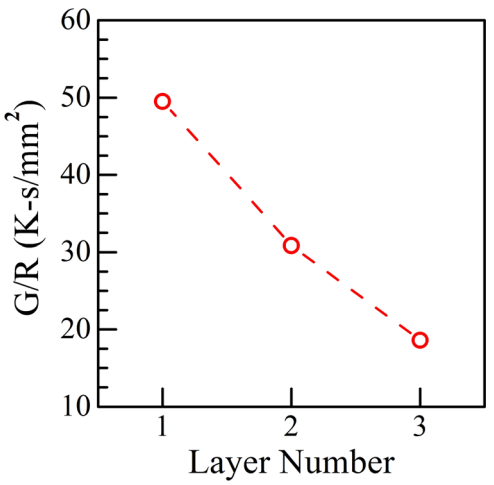

FIG. 7. Variation of the computed values of the solidification parameter G/R, where G is the growth velocity and R is the temperature gradient.

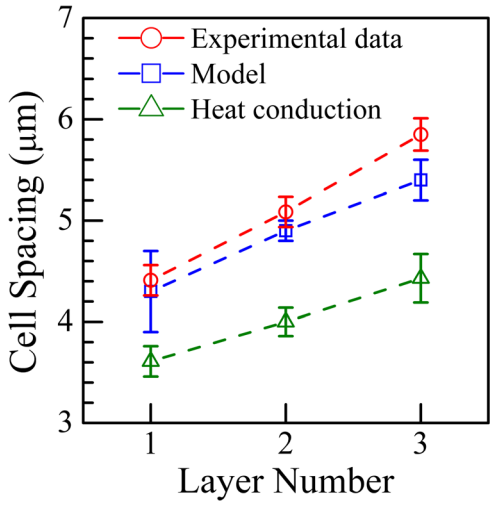

FIG. 8. Comparison of the computed cell dimension in different layers with those reported in the literature.[13]

where ΔT_E is the equilibrium solidification temperature range and D_L is the solute diffusion coefficient. For a given alloy, G/R defines the stability of the solidification front. Figure 7 shows that the computed value of G/R decreases along the build height since the temperature gradient reduces in the upper layers because of heat buildup. The computed value of G/R decreases from 49.5 (K s)/mm^2 in the first layer to 18.6 (K s)/mm^2 in the third layer. The value of ΔT_E for the stainless steel is 40 K and D_L for Cr diffusivity in liquid steel is about 5×10^{-3} mm^2/s. The resulting $\Delta T_E/ D_L$ of 8×10^4 (K s)/mm^2 is much higher than the computed values of G/R in all the layers. Thus, a plane solidification front is unstable and the variation of G/R shows that solidification will occur with progressively lower stability of plane front in the upper layers. The solidification structure will be either cellular or dendritic.

Figure 8 shows the computed variation of the average cell spacing in different layers. The cell spacing increases towards the upper layers from 4.5 μm in the first layer to 6 μm in the third layer due to the reduction in the cooling rate at the solidification front. The cell spacings computed using the cooling rates obtained from the conduction based models are much lower than the experimentally observed values[13] and varied from 3.5 μm to 4.5 μm from the first to the third layer. Thus, the convective heat transfer calculations provide much more realistic cell spacings than the heat conduction model.

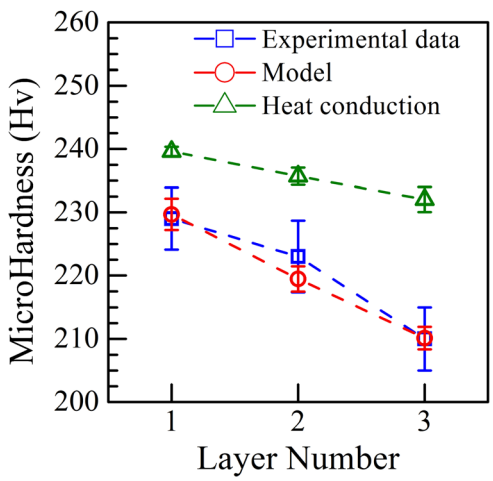

FIG. 9. Computed and the experimentally determined hardness values[13] in three layers.

Figure 9 shows the decrease in the computed hardness value towards the top layer owing to an increase in the cell spacing. The computed hardness decreases from 230 MPa in the first layer to 209 MPa in the third layer. These values are lower than the values computed from an independent investigation using a heat conduction model[13] and agree much more closely with the independent experimental results.[13]

V. CONCLUSIONS

A three-dimensional, transient, heat transfer, and fluid flow model is developed and tested for the laser assisted deposition of a multilayer structure from coaxially fed austenitic stainless steel powder. The layer wise evolution of temperature and velocity fields and melt pool geometry is examined for a three layered structure.

The computed melt pool geometry agreed well with the corresponding independent experimentally measured results. Both the computed results and the experimentally determined built geometry showed a slight increase in the melt pool size towards the upper layers.

The computed cooling rates decreased progressively with the addition of new layers. The cooling rates decreased from about 6550 K/s in the first layer to about 2780 K/s in the third layer. These results are in agreement with the independently observed changes in the solidification structure. Both the independently observed coarsening of the cell structure and the consequent decrease in the hardness of the deposited material in the upper layers agree well with the computed variation of cooling rates in different layers.

The computed cell spacings from the computed cooling rates and empirical equations available in the literature were in the range of 4–6 μm. These values agreed well with independent experimentally determined results. The hardness values computed using the computed cooling rates agreed fairly well with the independent experimentally determined results.

The results show that ignoring convection in the liquid pool results in unrealistically high cooling rates and the use of heat transfer and fluid flow model provides much more reliable results of cooling rates, cell spacings, and hardness than those obtained using a heat conduction model.

[1]D. D. Gu, W. Meiners, K. Wissenbach, and R. Poprawe, Int. Mater. Rev. **57**, 133 (2012).
[2]G. P. Dinda, A. K. Dasgupta, and J. Mazumder, Mater. Sci. Eng., A **509**, 98 (2009).
[3]L. Song, V. Bagavath-Singh, B. Dutta, and J. Mazumder, Int. J. Adv. Manuf. Technol. **58**, 247 (2012).
[4]K. Zhang, W. Liu, and X. Shang, Opt. Laser Technol. **39**, 549 (2007).
[5]M. L. Griffith, L. D. Harwell, J. T. Romero, E. Schlienger, C. L. Atwood, and J. E. Smugeresky, in *Proceeding of the 6th Solid Freeform Fabrication Symposium, Department of Mechanical Engineering, University of Texas, Austin, Texas, August 11–13* (1997), p. 387.
[6]X. He and J. Mazumder, J. Appl. Phys. **101**, 053113 (2007).
[7]H. Qi, J. Mazumder, and H. Ki, J. Appl. Phys. **100**, 024903 (2006).

[8]P. Peyre, P. Aubry, R. Fabbro, and R. Neveu, J. Phys. D: Appl. Phys. **41**, 025403 (2008).
[9]A. V. Gusarov and J.-P. Kruth, Int. J. Heat Mass Transfer. **48**, 3423 (2005).
[10]W. Hofmeister, M. Wert, J. Smugeresky, J. Philliber, M. Griffith, and M. Ensz, J. Min. Met. Mat **51**, 1 (1999).
[11]M. L. Griffith, M. T. Ensz, J. D. Puskar, C. V. Robino, J. A. Brooks, J. A. Philliber, J. E. Smugeresky, and W. H. Hofmeister, MRS Proc. **625**, 9 (2000).
[12]V. Neela and A. De, Int. J. Adv. Manuf. Technol. **45**, 935 (2009).
[13]V. D. Manvatkar, A. A. Gokhale, G. Jagan Reddy, A. Venkataramana, and A. De, Metall. Mater. Trans. A **42**, 4080 (2011).
[14]L. Wang and S. Felicelli, J. Manuf. Sci. Eng. **129**, 1028 (2007).
[15]S. M. Kelly and S. L. Kampe, Metall. Mater. Trans. A **35**, 1861 (2004).
[16]M. L. Griffith, M. E. Schlinger, L. D. Harwell, M. S. Oliver, M. D. Baldwin, M. T. Ensz, M. Essien, J. Brooks, C. V. Robino, J. E. Smugeresky, W. H. Hofmeister, M. J. Wert, and D. V. Nelson, Mater. Des. **20**, 107 (1999).
[17]L. Costa, R. Vilar, T. Reti, and A. M. Deus, Acta. Mater. **53**, 3987 (2005).
[18]M. Grujicic, Y. Hu, G. M. Fadel, and D. M. Keicher, J. Mater. Synth. Process. **9**, 223 (2001).
[19]S. Wen and Y. C. Shin, J. Appl. Phys. **108**, 044908 (2010).
[20]S. Wen and Y. C. Shin, Int. J. Heat Mass Transfer. **54**, 5319 (2011).
[21]S. Morville, M. Carin, P. Peyre, M. Gharbi, D. Carron, P. L. Masson, and R. Fabbro, J. Laser Appl. **24**, 032008 (2012).
[22]F. Kong and R. Kovacevic, Metall. Mater. Trans. B **41**, 1310 (2010).
[23]A. Raghavan, H. L. Wei, T. A. Palmer, and T. DebRoy, J. Laser Appl. **25**, 052006 (2013).
[24]S. V. Patankar, *Numerical Heat Transfer and Fluid Flow* (McGraw-Hill, New York, 1982).
[25]W. Zhang, G. G. Roy, J. W. Elmer, and T. DebRoy, J. Appl. Phys. **93**, 3022 (2003).
[26]W. Zhang, C. H. Kim, and T. DebRoy, J. Appl. Phys. **95**, 5220 (2004).
[27]K. C. Mills, *Recommended values of Thermophysical Properties for Selected Commercial Alloys* (Cambridge, England, 2002).
[28]J. Lin, Opt. Laser Technol. **31**, 565 (1999).
[29]G. H. Geiger and D. R. Poirier, *Transport Phenomena in Metallurgy* (Addison-Wesley, USA, 1973).
[30]B. Zheng, Y, Zhou, J. E. Smugeresky, J. M. Schoenung, and E. J. Lavernia, Metall. Mater. Trans. A **39**, 2237 (2008).
[31]J. R. Cahoon, W. H. Broughton, and A. R. Kutzak, Metall. Trans. **2**, 1979 (1971).
[32]G. E. Dieter, *Mechanical Metallurgy*, 3rd ed. (McGraw Hill Book Co., Singapore, 1998).
[33]B. P. Kashyap and K. Tangri, Acta Metall. Mater. **43**, 3971(1995).
[34]D. Tabor, Rev. Phys. Technol. **1**, 145 (1970).